

# A molecular interaction-diffusion framework for predicting organic solar cell stability

Masoud Ghasemi<sup>1,2</sup>, Nrup Balar<sup>1,3</sup>, Zhengxing Peng<sup>1</sup>, Huawei Hu<sup>1,3</sup>, Yunpeng Qin<sup>1</sup>, Taesoo Kim<sup>2</sup>, Jeromy J. Rech<sup>1,3</sup>, Matthew Bidwell<sup>1,5</sup>, Walker Mask<sup>6</sup>, Iain McCulloch<sup>7,8</sup>, Wei You<sup>1,5</sup>, Aram Amassian<sup>1,5</sup>, Chad Risko<sup>1,6</sup>, Brendan T. O'Connor<sup>1,5</sup> and Harald Ade<sup>1,5</sup>

Rapid increase in the power conversion efficiency of organic solar cells (OSCs) has been achieved with the development of non-fullerene small-molecule acceptors (NF-SMAs). Although the morphological stability of these NF-SMA devices critically affects their intrinsic lifetime, their fundamental intermolecular interactions and how they govern property-function relations and morphological stability of OSCs remain elusive. Here, we discover that the diffusion of an NF-SMA into the donor polymer exhibits Arrhenius behaviour and that the activation energy  $E_a$  scales linearly with the enthalpic interaction parameters  $\chi_H$  between the polymer and the NF-SMA. Consequently, the thermodynamically most unstable, hypo-miscible systems (high  $\chi$ ) are the most kinetically stabilized. We relate the differences in  $E_a$  to measured and selectively simulated molecular self-interaction properties of the constituent materials and develop quantitative property-function relations that link thermal and mechanical characteristics of the NF-SMA and polymer to predict relative diffusion properties and thus morphological stability.

he power conversion efficiency (PCE) of organic solar cells (OSCs) is now approaching commercial viability thanks to the development of non-fullerene-small molecule acceptors (NF-SMAs)<sup>1</sup>. Although the intrinsic morphological stability of OSC materials critically affects the lifetime and burn-in of devices<sup>2-5</sup>, the fundamental molecular interactions and property-function relations that govern morphological stability of these non-fullerene OSCs have yet to be revealed. A detrimental deviation from a device-optimized morphology can happen through two primary scenarios: (1) thermodynamic relaxation of the mixed domains in the blend from an initially quenched composition to the binodal<sup>6,7</sup> or (2) by nucleation, growth and coarsening of crystalline acceptor domains resulting in depletion of NF-SMA in surrounding regions with a composition limit determined by the liquidus<sup>8,9</sup>. While a certain amount of mixed amorphous phases (with a composition near the percolation threshold) is crucial for efficient charge separation and extraction, a donor-acceptor miscibility that is too low (hypo-miscible) can lead to performance deteriorations due to over-purification of mixed domains over time<sup>6,10,11</sup>. A miscibility that is too high (hyper-miscible) leads to a low intrinsic performance of OSCs due to insufficient phase separation<sup>12–15</sup>. The relationship between miscibility and NF-SMA volume fraction is expressed through a phase diagram (Fig. 1a) that can be parameterized by the Flory-Huggins interaction parameter  $\chi$ . In its generalized form,  $\chi$  is described as the sum of enthalpic ( $\chi_H$ ) and entropic ( $\chi_S$ ) components via  $\chi = \chi_S + \chi_H$ , where  $\chi_S = A$  and  $\chi_H = B/T$ , with A and B being system-dependent constants and T being the absolute temperature. While some polymer:NF-SMA combinations exhibit good heat-stress resistance or shelflife device stability<sup>3,16</sup>, record-holding Y6 and its derivatives do not lead to stable morphologies in binary

blends<sup>17,18</sup>. The mechanisms behind these stability characteristics remain unexplained.

To establish and delineate quantitative property-function relations that can predict morphological stability, we evaluate the thermodynamic drivers (such as miscibility,  $\chi(T)$ ) and kinetic factors (including diffusion coefficients, activation energies) of hypo-miscible polymer:NF-SMA systems spanning a wide range of performance and stability. Hyper-miscible blends that are intrinsically low performing are not explored<sup>10,13</sup>. The NF-SMAs (Y6, EH-IDTBR, di-PDI, IT-M, IEICO-4F) and donor polymers (P3HT, FTAZ, PTB7-Th, PBDB-T, PBDB-T2F also known as PM6) included here are extensively used in state-of-the-art OSCs, yet also span a reasonable range of structural and chemical motifs (see Methods for full materials names). To understand morphological stability, we determine the miscibility gap ( $\phi_{\mathbb{B}}$ , binodal composition) and reveal that the most stable systems are the most hypo-miscible ones. This contradicts previous models, as these hypo-miscible systems should be highly unstable<sup>6,7,19</sup>. Since morphological stability is predicated on limited molecular rearrangements, we determine the temperature-dependent diffusion coefficients D(T) of the SMAs and observe thermally activated Arrhenius diffusion. Large differences in diffusion coefficients at 85 °C ( $D_{85}$ ) of around 11 orders of magnitude across different polymer:NF-SMA combinations are observed, which increases to roughly 12 orders of magnitude if the historic fullerene acceptor reference system P3HT:PCBM is considered<sup>20</sup>. We discover that the activation energy  $E_a$  of diffusion scales with the net material exchange enthalpy  $\chi_H$ . Additional property-function relationships are identified by using easily measurable parameters that are proxies for molecular self-interactions, including the elastic modulus  $(E_{\rm F})$  of the donor polymers and the

<sup>1</sup>Department of Physics and Organic and Carbon Electronics Laboratories (ORaCEL), North Carolina State University, Raleigh, NC, USA. <sup>2</sup>Department of Materials Science and Engineering and Organic and Carbon Electronics Laboratories (ORaCEL), North Carolina State University, Raleigh, NC, USA. <sup>3</sup>Department of Mechanical and Aerospace Engineering and Organic and Carbon Electronics Laboratories (ORaCEL), North Carolina State University, Raleigh, NC, USA. <sup>4</sup>Department of Chemistry, University of North Carolina at Chapel Hill, Chapel Hill, NC, USA. <sup>5</sup>Department of Chemistry and Centre for Plastic Electronics, Imperial College London, London, UK. <sup>6</sup>Department of Chemistry and Center for Applied Energy Research, University of Kentucky, Lexington, KY, USA. <sup>7</sup>King Abdullah University of Science and Technology (KAUST), KAUST Solar Center, Physical Sciences and Engineering Division, Thuwal, Saudi Arabia. <sup>8</sup>Department of Chemistry, Chemistry Research Laboratory, University of Oxford, Oxford, UK. <sup>12</sup>e-mail: btoconno@ncsu.edu; hwade@ncsu.edu

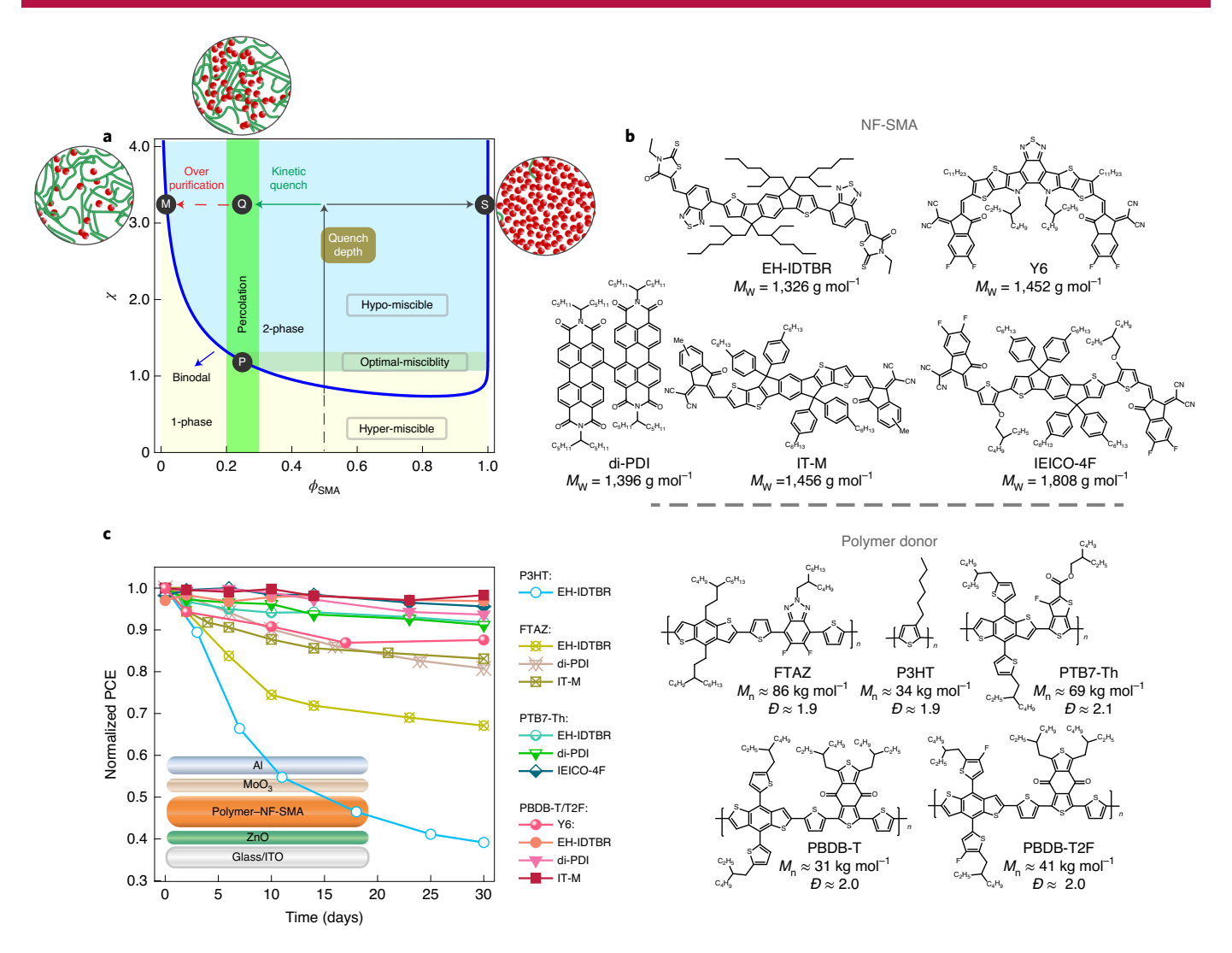


**Fig. 1** | Phase diagram, chemical structure, schematic of the device structure and degradation of polymer:NF-SMA devices.  $\mathbf{a}$ ,  $\chi - \phi_{\rm g}$  phase diagram with the binodal separating the one- and two-phase regions. For most material combinations, the ideal composition of the amorphous, mixed domains in the devices is near the percolation threshold. Only hypo-miscible blends can reach that threshold and have a multiphasic bulk hetero-junction morphology. The points P, Q, M and S represent the percolation threshold composition of the SMA in the mixed domains at equilibrium (P), quenched mixed phase with a percolation threshold composition (Q), equilibrium mixed phase (M) and nearly pure SMA phase (S). **b**, Chemical structures of the polymers and the NF-SMAs used in this study including the molecular weight ( $M_w$ ) of the NF-SMAs, and number-averaged molecular mass ( $M_n$ ) of the polymers and polydispersity (D). **c**, Normalized PCE versus time of polymer:NF-SMA devices to assess shelflife of the devices stored in the dark at room temperature in a nitrogen-filled glovebox. The PCE is normalized by the highest measured efficiency. Inset, schematic of the inverted device structure.

glass transition temperature ( $T_{\rm g}$ ) of the NF-SMAs. The  $\chi_{\rm H}$  scales linearly with  $T_{\rm g}$  of the NF-SMA and  $E_{\rm F}$  of the polymer, whereas the diffusion coefficients decrease exponentially with increasing  $T_{\rm g}$  and  $E_{\rm F}$ . This insight provides a framework that connects thermodynamics and kinetics, and allows new materials to be prescreened for stability using simple thermal and mechanical measurements. Molecular dynamics simulations that predict  $T_{\rm g}$  and  $E_{\rm F}$  open up an additional avenue for evaluating the stability of new materials before their synthesis.

#### Device fabrication and shelflife

The chemical structures of the donor polymers and NF-SMAs used are shown in Fig. 1b. The PCE versus time (shelflife) of 11 OSCs based on these materials is provided in Fig. 1c. Details of these results and processing conditions are documented in the Methods section and Supplementary Information, and summarized in Supplementary Tables 1 and 2. Overall, the performance confirms the wide range of intrinsic shelflife observations made previously<sup>2,4,21</sup>. In addition,

performance and shelflife are provided as a function of annealing temperature for select systems (Supplementary Figs. 1 and 2) to further illustrate the morphological instability of these devices. Using the device stability data as a guide and motivation, we can now study and relate thermodynamic, diffusion, thermal and mechanical properties and establish morphological stability correlations.

#### Miscibility gap and its relation to stability

To relate thermodynamic and diffusion properties, we use secondary ion mass spectrometry (SIMS) interdiffusion experiments on polymer:NF-SMA bilayers,  $^{10,13,20,22}$  with Fig. 2a displaying di-PDI diffusion profiles into a PTB7-Th polymer film as an illustrative example. More than 80 diffusion concentration profiles C(x,t) obtained at different temperatures are fitted using concentration-independent and -dependent one-dimensional (1D) solutions of Fick's second law. From such traces and fits, we first deduce the miscibility gap  $\phi_B(T)$  (Supplementary Information, Supplementary Figs. 3–8 and Supplementary Table 4)7. Examples of

NATURE MATERIALS ARTICLES

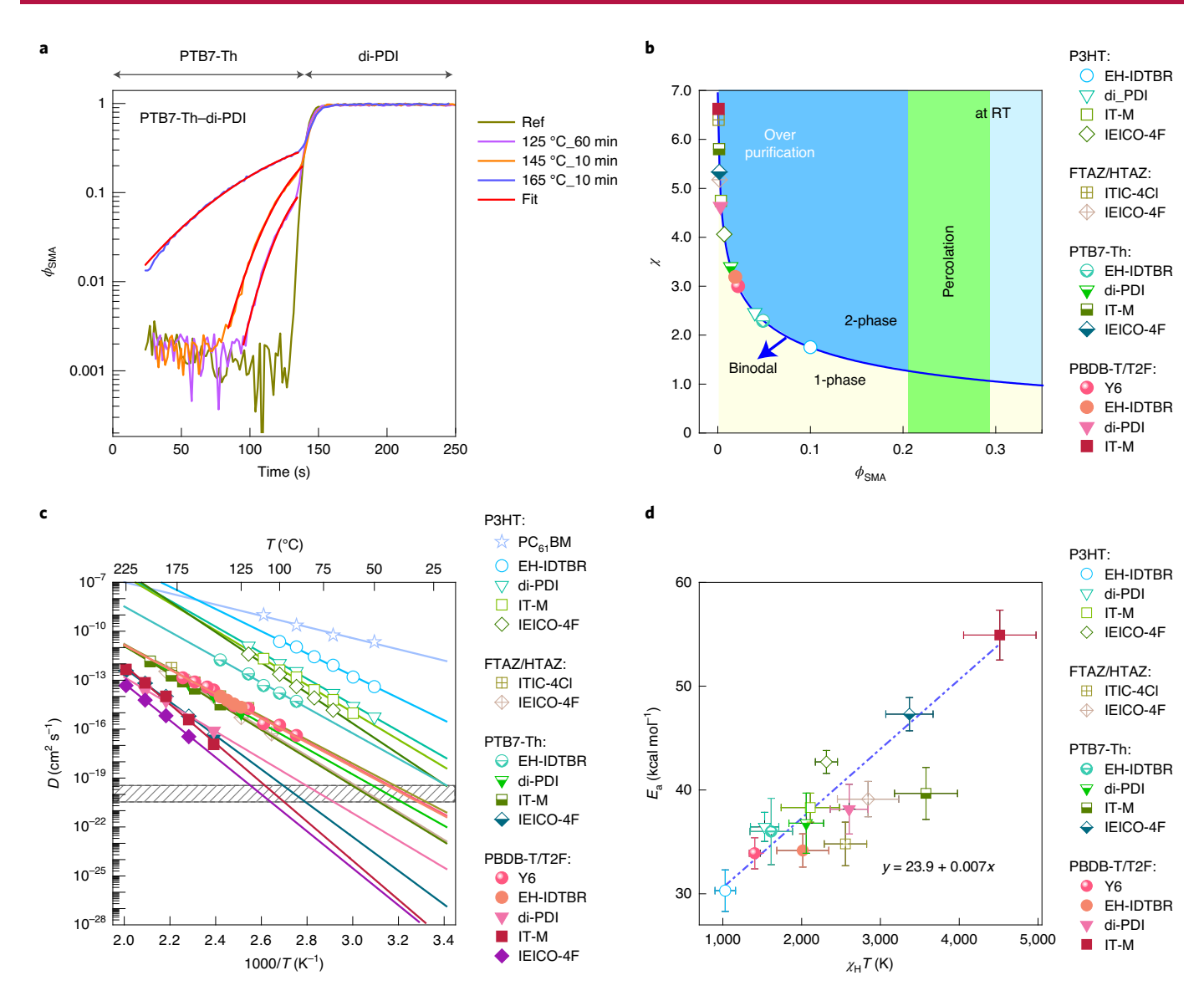


**Fig. 2 | SIMS** profiles, phase diagram, diffusion properties and activation energy of polymer:NF-SMA. a, Fits using 1D solution of Fick's second law (red lines) for PTB7-Th:di-PDI at temperatures as indicated. The complete set of SIMS profiles for all temperatures and thier fits to Fick's law for the concentration of the SMA in the polymer layer can be found in the Supplementary Information.  $\mathbf{b}$ ,  $\chi - \phi_B$  phase diagram with  $\chi_{(RT)}$  exemplifying the results. The region delineated by the binodal and the percolation threshold corresponds to over-purified mixed domains. Due to hypo-miscibility of all the systems, some of the symbols overlap when plotting on the binodal curve.  $\mathbf{c}$ , Temperature-dependent diffusion coefficient D(T) of different polymer:NF-SMA systems fitted by an Arrhenius relation. The time and temperature combinations that can be assessed with SIMS are limited by the finite thickness imposed by the SIMS measurement and the time before the NF-SMA reaches equilibrium throughout the film. To provide additional context, our SIMS data was supplemented with literature data for P3HT:PC $_{61}$ BM (ref.  $^{20}$ ). The horizontal dashed box delineates the diffusion coefficient for an acceptor molecule to diffuse 20 nm on a time scale of 1 to 10 years.  $\mathbf{d}$ ,  $E_a$  versus  $\chi_H T$  correlation analysis. The correlation observed indicates that  $E_a$  also scales with  $\chi_H$  at any given T. The error bars on  $E_a$  and  $\chi_H$  values are extracted from fit parameters and the error on each value.

these results are presented in Fig. 2b for  $\chi_{\rm (RT)}$  and compared against the percolation threshold of the NF-SMA in the polymer indicated by the green band of roughly 20–30% v/v (refs. <sup>23–25</sup>). This composition range is typically the lowest acceptable concentration in the mixed domains for good performance. Specifically, PBDB-T:IT-M, PTB7-Th:IT-M and PTB7-Th:IEICO-4F have extremely low  $\phi_{\rm B}(T)$  of approximately 1–3% v/v, yet, some of these hypo-miscible systems are among the highest efficiency OSCs<sup>26</sup>. PBDB-T2F:Y6 system with over 15% reported PCE<sup>17</sup> is also a hypo-miscible system. The hypo-misciblity indicates that these systems have to be kinetically quenched to a non-equilibrium mixed domain composition<sup>23</sup>. If kinetically possible, diffusion-enabled demixing of the morphol-

ogy would lead to over-purification and severe burn-in. To our surprise, the most hypo-miscible systems, namely PBDB-T:IT-M and PTB7-Th:IEICO-4F, show excellent shelflife that is superior to that of the less hypo-miscible systems including PBDB-T2F:Y6.

#### **Extracting diffusion properties and interaction parameter**

To delineate why some of the most thermodynamically unstable devices can still exhibit strong morphological stability, we extract the diffusion properties of these systems from portions of the SIMS profiles as delineated in the Supplementary Information. Large variations in D(T) are observed (Fig. 2c) revealing thermally activated (Arrhenius) diffusion with

$$D(T) = D_0 \exp\left(-\frac{E_a}{kT}\right) \tag{1}$$

where  $E_{\rm a}$  is the diffusion enthalpy/activation energy and  $D_{\rm 0}$  is the intrinsic diffusion coefficient at infinite temperature or zero  $E_{\rm a}$ . Fitting to this relation yields  $E_{\rm a}$  for the diffusion of NF-SMAs into the polymer hosts and allows for estimation of D(T) at lower device operating temperatures by extrapolation (Supplementary Table 5). The activation energies range from 13 to 54.9 kcal mol<sup>-1</sup> (0.56 to 2.38 eV) and are significantly larger than thermal energy (kT around 26 meV).  $PC_{\rm 61}BM$  in P3HT has the highest diffusion coefficient and the lowest  $E_{\rm a}$  among all polymer:SMA systems compared here. In contrast, IT-M in PBDB-T has a very low diffusion coefficient and the highest activation energy. At 85 °C, these two extreme systems have extrapolated diffusion coefficients of  $2.0 \times 10^{-10}$  and  $2.7 \times 10^{-22} \, {\rm cm}^2 \, {\rm s}^{-1}$ , respectively, a difference of 12 orders of magnitude. A trend emerges in which some of the most stable systems have the highest  $E_{\rm a}$ .

To reveal the underlying relation behind diffusion and thermodynamic properties, we extract  $\chi_{\rm S}$  and  $\chi_{\rm H}$  (see Supplementary Information for details on system selection constraints and  $\chi(T)$ extraction) and discover that  $E_a$  and  $\chi_H T$  are correlated (Fig. 2d). The observed  $E_a - \chi_H$  correlation indicates that  $E_a$  also scales with  $\chi_{\rm H}$  at any given T and that the diffusion activation has an underlying thermodynamic contribution or cause. To establish relations underlying the material properties, we note that  $\chi_{\rm H}$  is proportional to  $\varepsilon_{\rm pp} - 2\varepsilon_{\rm ps} + \varepsilon_{\rm ss}$  (where the  $\varepsilon$  are the pair-wise enthalpic energies between two constituent polymer segments (p) and/or small molecules (s) on a lattice) $^{27,28}$  and we endeavour to test the impact of the self-interaction energies  $\varepsilon_{\rm pp}$  and  $\varepsilon_{\rm ss}$  on  $E_{\rm a}$  and D. To assist in determining the role of the self-interaction energies, we evaluate material properties that can be readily determined experimentally and can be related to the cohesive energy density (CED), which is proportional to  $\varepsilon$  (refs. <sup>29,30</sup>). Specifically, we are inspired that the elastic modulus has been observed to scale linearly with CED in glassy polymers<sup>31</sup> and small molecules<sup>32</sup>, and  $T_g$  scales linearly with CED/n, where n is the number of molecular oscillators of the polymer<sup>30</sup>.

## Thermal transitions of NF-SMAs and stiffness and relaxation of donor polymers

We elucidate the molecular self-interactions of the NF-SMAs by characterizing their thermal properties with differential scanning calorimetry (DSC) (Fig. 3a). For the NF-SMAs considered, di-PDI is the only material that exhibits a directly measurable  $T_{\rm g}$  of 137 °C. All other NF-SMAs exhibit exothermal cold crystallization. For the mobility of the SMAs to allow crystallization on heating indicates that cold crystallization temperature ( $T_{\rm c}$ ) will be similar to the respective  $T_{\rm g}$ , and the cold crystallization signal probably obscures the  $T_{\rm g}$  signature. Y6 has the lowest  $T_{\rm c}$  (roughly 105 °C), followed by EH-IDTBR, IT-M and IEICO-4F with  $T_{\rm c}$  at roughly 113, 179 and 196 °C, respectively. We will use  $T_{\rm c}$  as a proxy for  $T_{\rm g}$  of the NF-SMA. The transition temperature of Y6 was confirmed using an ultraviolet-visible spectroscopy technique that yields 102 °C for Y6 and 116 °C for EH-IDTBR (Supplementary Fig. 9)<sup>33</sup>.

Except for P3HT, the donor polymers do not show a clear  $T_{\rm g}$ , neither do they exhibit a melting transition associated with crystal-linity as measured by DSC. These results are in line with dynamic mechanical analysis (DMA) results (Supplementary Fig. 10). The DMA reveals thermal relaxations between -30 and  $-10\,^{\circ}{\rm C}$  that are indicative of viscoelasticity at room temperature, yet cannot be clearly attributed to a  $T_{\rm g}$  (refs.  $^{34,35}$ ). To distinguish the polymers' viscoelasticity we consider their relaxation behaviour  $^{36-38}$ . The stress relaxation behaviour was characterized by a relaxation time  $(\tau_{\rm r})$  extracted from fitting a Kohlrausch–Williams–Watts (KWW) model (Fig. 3b and Supplementary Figs. 11 and 12). While caution

should be taken in the physical interpretation of  $\tau_r$  (ref.  $^{39}$ ), it accurately captures the observed behaviour that P3HT relaxes the quickest, followed by FTAZ, PTB7-Th, PBDB-T2F and PBDB-T.

Since the molecular self-interactions of the polymers could not be probed with DSC and since DMA measurements show complex thermal behaviour, we investigate the elastic modulus ( $E_{\rm F}$ ) as a proxy for self-interactions<sup>31,32,40</sup> using a wrinkling metrology approach (Supplementary Fig. 13)<sup>41</sup>.  $E_{\rm F}$  of a polymer does depend on molecular weight but typically plateaus above the entanglement molecular weight but typically plateaus above the entanglement molecular weight<sup>35,42</sup>. PBDB-T2F and PBDB-T films exhibited the highest stiffness with  $E_{\rm F}$  of  $0.84 \pm 0.10$  GPa, followed by PTB7-Th and FTAZ with  $E_{\rm F}$  of  $0.55 \pm 0.05$  and  $0.37 \pm 0.08$  GPa, respectively.  $E_{\rm F}$  of P3HT of similar molecular weight has been shown to be approximately  $0.20 \pm 0.02$  GPa, whereas  $E_{\rm F}$  of regio-random (amorphous) P3HT is reported to be 0.013 GPa (ref. <sup>43</sup>). The elastic modulus of the films is summarized in the inset of Fig. 3b.

#### Correlation analysis

Correlation analysis reveals that the  $T_g$  of a NF-SMA has a strong and quantifiable impact on  $\chi_H T$  as shown in Fig. 4a for the three polymers (P3HT, PTB7-Th and PBDB-T) and by extension to  $E_a$ . Similarly, the elastic modulus  $E_{\rm E}$  of the polymers also has an effect on  $\chi_{\rm H}$  and  $E_{\rm a}$  for a given NF-SMA (Fig. 4c). Considering that NF-SMA diffusion takes place in the polymer amorphous phase only, we use the tensile modulus of amorphous regio-random P3HT (13 MPa) to present the relations between  $\chi_{\rm H}$  (ref. 44) and  $E_{\rm P}$  Furthermore, the impact of  $T_g$  and  $E_F$  on the diffusion coefficient can be observed when considering diffusion at 85 °C (a temperature specified in industrial stability standard ASTM E1171, ref. 45) as an example (Fig. 4b,d). A strong dependence of  $D_{85}$  on the constituent materials separates into groups that relate to each other. Along the  $T_g$  dimension, an exponential decrease of  $D_{85}(T_g)$  is observed for binaries related to a given polymer. Similarly, an exponential decrease of  $D_{85}(E_{\rm F})$  is observed for binaries related to a given NF-SMA. These correlations and fitted functions are summarized in Supplementary Table 9.

When considering the above correlations, a coherent framework emerges that interrelates morphological stability, activation energies, interaction parameter, diffusion properties and mechanical or thermal properties, which in turn are governed by intermolecular interactions (Table 1). The conceptual relations of the various equilibrium and dynamic parameters correlated above and their underlying homo- or hetero- molecular interactions are summarized in Table 2.

Fundamentally, the underlying thermodynamic  $(\chi)$ , kinetic (D), thermal  $(T_e)$  and mechanical  $(E_F)$  and  $\tau_r$ ) properties and phenomena are critically affected by intermolecular interactions. When analysing the relations captured in Fig. 4a,c, not only is there a strong correlation of  $\chi_H$  with polymer and NF-SMA material properties, but also, each correlation clearly shows differentiation on the basis of the NF-SMA or polymer type, respectively. This indicates that the various  $\Delta S$  and  $\Delta H$  parameters in Table 2 have a connection and common contribution, although conceptually they are not necessarily the same. To advance an interpretation, we consider a first-order model and draw on a relation observed in a range of commodity polymers where  $T_g$  has been shown to be linearly related to CED/n (refs. <sup>29,30</sup>). Given that  $\chi_{\rm H}$  is a linear function of  $\varepsilon_{\rm ss}$  and thus CED<sub>ss</sub>, the observed linear relations between  $\chi_{\rm H}$  and  $T_{\rm g}$  indicate that  $T_{\rm g}$  of the NF-SMA is a good proxy for  $\varepsilon_{ss}$  and that the number of molecular oscillators in the NF-SMAs investigated are effectively the same. Since many of the conjugated polymers do not show a clear  $T_e$ , using the approach used for the NF-SMA cannot be extended to the polymers considered. Instead, we find a linear relationship between  $\chi_{\rm H}$  and  $E_{\rm F}$  (Fig. 4c) indicating that  $E_{\rm F}$  of the polymer is a reasonable proxy for  $\varepsilon_{\rm pp}$  and CED  $_{\rm pp}$  consistent with previous observations that  $E_{\rm F}$  scales with CED in small molecules<sup>32</sup> and glassy polymers<sup>31</sup>. Within this model in which  $\varepsilon_{ss}$  and  $\varepsilon_{pp}$  are linear functions of  $T_g$  of NATURE MATERIALS ARTICLES

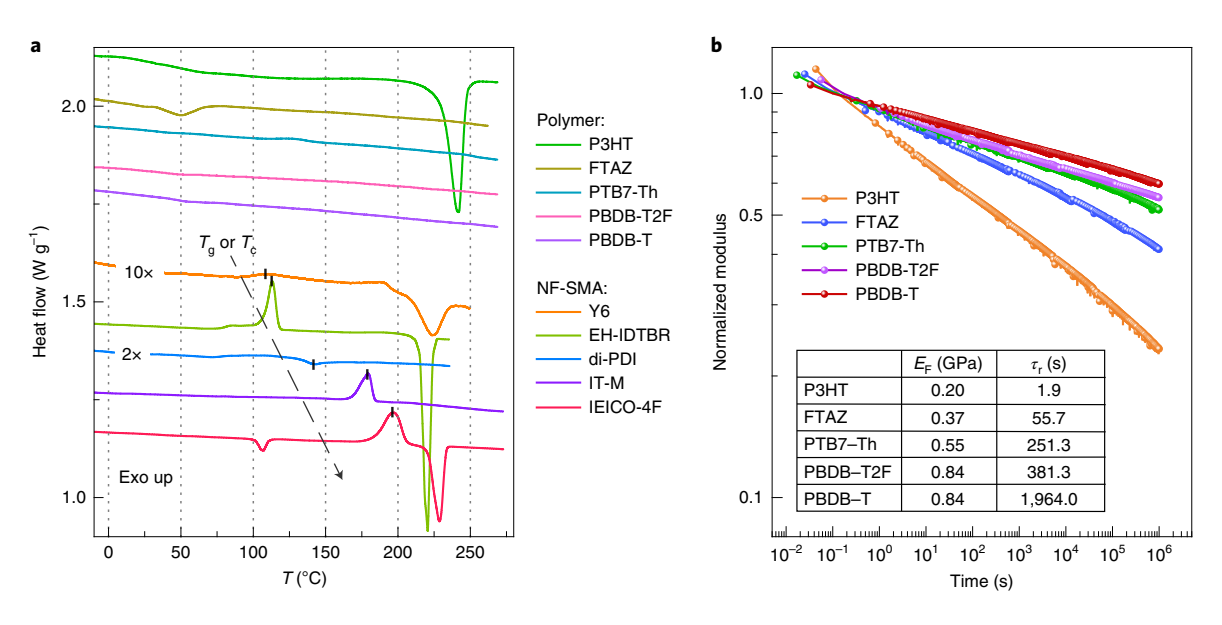


**Fig. 3 | Thermal and mechanical properties of neat polymers and neat NF-SMAs. a**, DSC thermograms of neat polymers and NF-SMAs collected from first heat with 10 and  $3^{\circ}$ C min<sup>-1</sup>, respectively. A higher heating rate ( $10^{\circ}$ C min<sup>-1</sup>) was used for polymers to increase the sensitivity of DSC signal. The traces are shifted vertically for better comparison and multiplied by two for di-PDI and by ten for Y6, to magnify transitions' features. The small melting peaks in FTAZ and IEICO-4F at roughly 50 and  $106^{\circ}$ C, respectively, are associated with side-chain crystallization that does not occur in as-cast thin films<sup>49</sup>. **b**, The normalized time-temperature-superposition (TTS) master curves of the stress relaxation modulus (normalized to the modulus value at 0.1s) of the neat polymer samples with a reference temperature of  $40^{\circ}$ C. The master curves were created by using shift factors fitted with the Williams-Landel-Ferry equation as given in the Supplementary Information. The inset of **b** shows the relaxation times ( $\tau_r$ ) and the fit parameters using KWW model, and the elastic modulus of neat polymers in GPa that were measured at room temperature.

the NF-SMA and  $E_{\rm F}$  of the polymer, respectively, we find consistency across the proxy parameters. For example, the observed offset by polymer type in the  $\chi_H$ - $T_{\rm g}$  correlations (Fig. 4a) indicates that  $\varepsilon_{\text{\tiny DD}}$  increases from P3HT to FTAZ, PTB7-Th and PBDB-T, which is supported by the  $\varepsilon_{pp}$  proxy of  $E_{\mathbb{P}}$ . When considering the dependence of diffusion on thermo-mechanical properties, a decreasing exponential correlation between of  $D_{85}$  and NF-SMA  $T_g$  and polymer  $E_F$ is observed, respectively. This is to be expected, as we simply see the contribution that the self-interaction ( $\varepsilon_{ss}$  or  $\varepsilon_{pp}$ ) makes to  $\chi_{H}$  and thus  $E_a$  and D. While the elastic modulus of polymers is dependent on a number of factors, particularly above its  $T_{\rm g}$ , the CED is a clear contributing factor as highlighted by the correlation of elastic modulus with  $\chi_{\mathrm{H}}$ . Furthermore, as the self-interaction  $\varepsilon_{\mathrm{pp}}$  decreases the segmental mobility of the chains should increase, which is reflected in an increase in stress relaxation (assuming similar molecular weight and free volume)<sup>37,46</sup>. The inferred comparative relation in  $\varepsilon_{pp}$  (P3HT < PTB7-Th < PBDB-T) is the same as the trend inferred from the activation energy analysis. Although we currently cannot infer the functional form of the relation to the polymer properties, the monotonic relations of D and  $\tau_r$  to molecular interactions are clear and indicate that  $\varepsilon_{\rm pp}$  and  $\varepsilon_{\rm ss}$  make significant, if not dominant, contributions to the diffusion and mechanical properties and the activation energy. Overall, we can conclude that  $T_{\rm g}$  of the NF-SMA and  $E_{\rm F}$  of the polymer are parameters that are controlled by the molecular self-interactions, which contribute to  $\chi_{\rm H}$  and thus to  $E_{\rm a}$ 

The deeper conceptual relations of the diffusion properties (D and  $E_{\rm a}$ ) to  $\chi_{\rm H}$ , and in turn to polymer  $E_{\rm F}$  and NF-SMA  $T_{\rm g}$ , now become clear. Diffusion is governed by equation (1) as shown in Table 2. Our results strongly indicate that  $\Delta H_{\rm d}$ , which is equal to  $E_{\rm a}$ , is scaling with  $\chi_{\rm H}$ . The very fact that there is an activation energy suggests that diffusion is not dominated by existing free volume (voids) in the materials. Rather, an additional void the size of the SMA needs to be created to allow the SMA to move. The energy associated with this thermally activated volume, in a pure polymer

or SMA phase, scales with the CED of these materials and the size of the free volume and thus  $\varepsilon_{\rm pp}$  and  $\varepsilon_{\rm ss}$ . It is particularly interesting to note that the activation of diffusion is a non-equilibrium process, yet, we can relate this activation to an equilibrium concept such as the  $\chi$  parameter,  $\varepsilon_{\rm pp}$ ,  $\varepsilon_{\rm ss}$  and  $\varepsilon_{\rm ps}$  and related proxy parameters that can be relatively easily measured.

The scaling relation of diffusion properties to the molecular self-interactions observed through  $T_{\rm g}$  opens up a simple route to provide synthetic guidance through simulations. We demonstrate this possibility here by using molecular dynamics simulations to assess the  $T_{\rm g}$  of EH-IDTBR, di-PDI, IT-M and IEICO-4F, for which values of 115, 134, 182 and 194 °C have been calculated, respectively; these values all track closely the experimental values observed (details for molecular dynamics simulations can be found in Methods and Supplementary Information).

Regarding the relation of the physical parameters measured to molecular structure, the current scaling relations in Fig. 4a,b to  $T_{\rm g}$  indicate that the molecular weight of the NF-SMA used and their molecular shape are similar enough to not be a dominating factor. This is an aspect that needs to be put into context. It is known that diffusion depends on molecular size and possibly shape<sup>48</sup>. Furthermore, the minimum size of an activated volume element that needs to be created has to be related to the size of the SMA. Although the details of the dependence of diffusion and stability on size, shape, degree of polymerization and possibly other characteristics of the chemical structure need to be researched further, our study suggests that increasing the size of the NF-SMA would yield improvements in stability.

Last, an important consideration is whether the diffusion coefficients measured here are relevant during casting or instabilities caused by purification or crystallization. The phase separation within the spinodal is governed by Cahn–Hillard theory. If the gradient energy term in Cahn–Hillard related to the interface tension is ignored, one can show that the generalized molecular mobility during demixing is proportional to *D*. Similarly, if crystallization

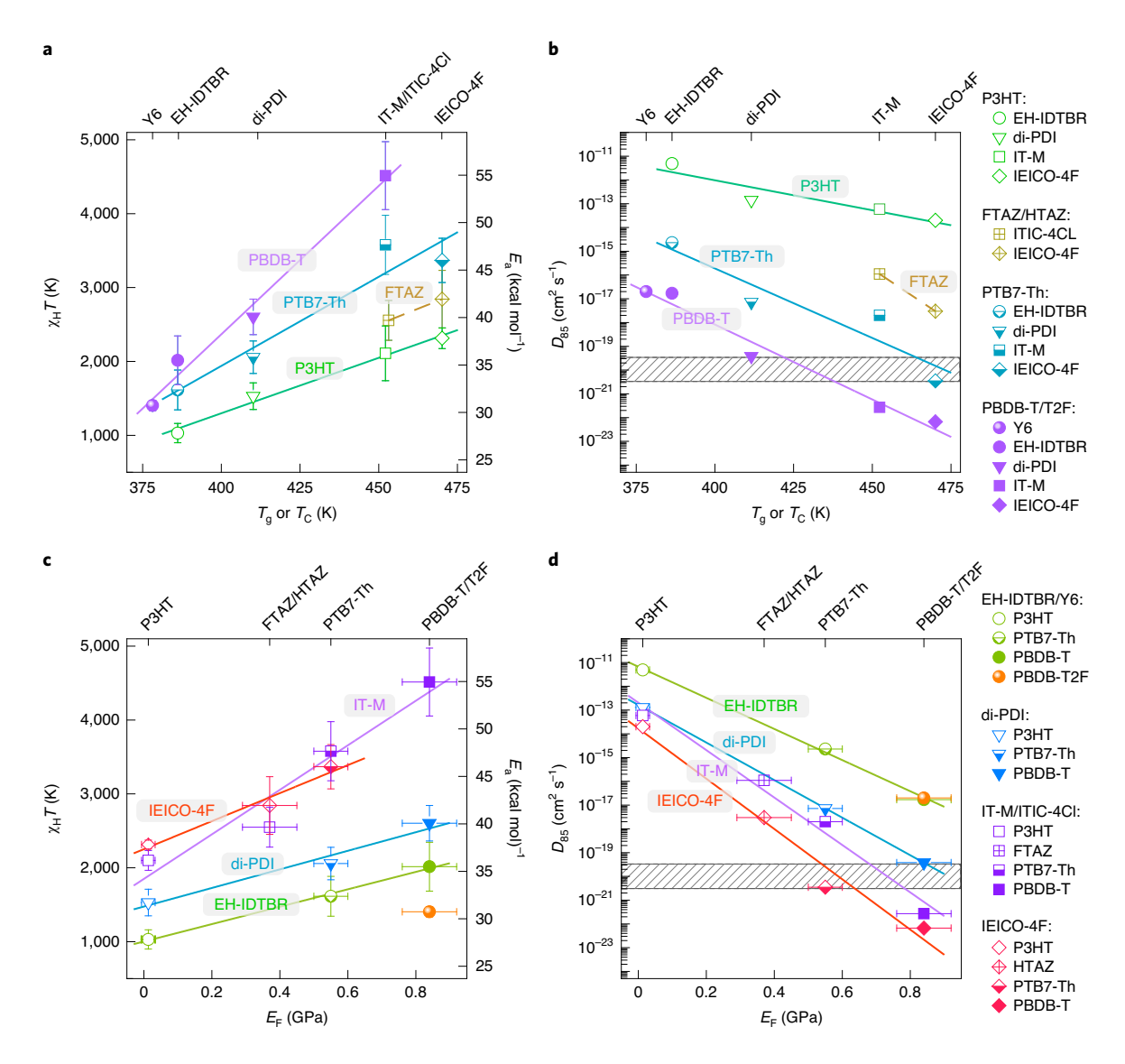


**Fig. 4 | Interrelations of parameters, with the**  $\chi$  and D dependence on  $T_g$  or  $T_c$  and  $E_F$ . **a**,  $\chi_H$  of P3HT:NF-SMA, PTB7-Th:NF-SMA and PBDB-T:NF-SMA systems as a function of NF-SMA's  $T_g$  or  $T_c$  as the proxy of  $T_g$ . The two FTAZ proxies also nicely fit the observed trends. **b**,  $D_{85}(T_g)$  of P3HT:NF-SMA, PTB7-Th:NF-SMA and PBDB-T:NF-SMA systems as a function of  $T_g$ . **c**,  $\chi_H$  of P3HT:NF-SMA, PTB7-Th-NF-SMA and PBDB-T:NF-SMA systems as a function of polymer  $E_F$ . **d**,  $D_{85}(E_F)$  of P3HT:NF-SMA, PTB7-Th:NF-SMA and PBDB-T:NF-SMA systems as a function of  $T_g$ . Note 85 °C is the temperature specified in industrial stability standard ASTM E1171 (ref. <sup>45</sup>). The error bars on  $\chi_H$  values are extracted from fit parameters, and  $E_F$  error bars were obtained from the first standard deviation of the elastic modulus and were calculated from at least three samples. The horizontal dashed boxes in **b** and **d** delineate the diffusion coefficient for an acceptor molecule to diffuse 20 nm on a time scale of 1 to 10 years.

causes device instability, the nucleation and growth factors of crystallization are both proportional to D. The diffusion coefficients measured and the observed differences are thus relevant to demixing, purification and crystallization; in short, these are relevant to devices and their fabrication and stability (see Supplementary Information for more details).

#### Outlook

One of the principal revelations is that  $E_{\rm a}$  scales with  $\chi_{\rm H}$ , and that  $\chi_{\rm H}$  is correlated with relatively easily measurable mechanical and thermal properties of the constituent materials that reflect self-interactions. Specifically,  $\chi_{\rm H}T$  and D scale linearly and exponentially, respectively, with the  $T_{\rm g}$  of the NF-SMA within a given series of polymers, and  $\chi_{\rm H}T$  and D scale linearly and exponentially, respectively, with  $E_{\rm F}$  of the polymer within a given series of NF-SMAs. Previously, it was inferred that an optimum miscibility or  $\chi$  has to be used to prevent

device degradation<sup>4,6</sup>. Our results reveal that highly hypo-miscible systems with large mixing enthalpy (high  $\chi_{\rm H}$ ) have high activation energy and low diffusion coefficient and thus provide an alternative—and indeed preferred—strategy to achieve long-term stability of OSCs by suppressing both demixing and crystallization. Yet, this approach may result in systems that have diminished mechanical resilience and a reduced processing window due to the need to quench the system into the optimal morphology.

Establishing firm relationships between diffusion, intermolecular interactions and chemical structure is expected to provide a rational design of materials for stability. Although more studies are necessary to reveal additional details, our results open up a new avenue of experimental approaches and computational simulations. Simple DSC, mechanical measurements and molecular dynamics simulations can be used to screen for molecular interaction and diffusion properties. We envision that a combination of measurements

NATURE MATERIALS

Table 1 | Summary of the system, kinetic and thermodynamic properties of materials and blends used to determine an activation

Blend	PCE <sub>max</sub> (%) fresh	PCE <sub>max</sub> (%) aged	χ <sub>H</sub> <b>T</b> ² (K)	$\chi_{S}^{a}$	$\chi_{(RT)}^{b}$	χ <sub>(85°C)</sub>	$D_{(85^{\circ}\text{C})}$ (cm <sup>2</sup> s <sup>-1</sup> )	E <sub>a</sub> (kcal mol⁻¹) <sup>c</sup>
P3HT:PC <sub>61</sub> BM <sup>d</sup>	-	-	-	-	-	-	2.0×10 <sup>-10</sup> (ref.	13.0
P3HT:EH-IDTBR	6.1	2.6	1,030	-1.7	1.8	1.2	$4.9 \times 10^{-12}$	30.3
P3HT:di-PDI	-	-	1,530	-2.8	2.3	1.5	$1.4 \times 10^{-13}$	36.5
P3HT:IT-M	-	-	2,110	-3.1	4.0	2.8	$5.9 \times 10^{-14}$	38.3
P3HT:IEICO-4F	-	-	2,315	-3.7	4.1	2.8	$1.9 \times 10^{-14}$	42.7
FTAZ:ITIC-4CI/FTAZ:IT-Me	11.8	9.5	2,556	-2.1	6.4	5.0	$1.1 \times 10^{-16}$	34.8
HTAZ:IEICO-4F	-	-	2,843	-4.4	5.2	3.6	$3.0 \times 10^{-18}$	39.1
PTB7-Th:EH-IDTBR	9.6	8.9	1,615	-3.1	2.3	1.4	$2.3 \times 10^{-15}$	36.0
PTB7-Th:di-PDI	5.3	4.8	2,058	-3.7	3.2	2.0	$7.8 \times 10^{-18}$	36.8
PTB7-Th:IT-M	7.9	7.6	3,578	-6.0	5.8	3.8	$2.0 \times 10^{-18}$	39.7
PTB7-Th:IEICO-4F	9.5	9.2	3,368	-6.2	5.3	3.4	$3.5 \times 10^{-21}$	47.3
PBDB-T2F:Y6	15.7	14.2	1,405	-1.5	3.0	2.2	$1.9 \times 10^{-17}$	33.9
PBDB-T:EH-IDTBR	8.4	8.4	2,015	-3.5	3.2	2.1	$1.7 \times 10^{-17}$	34.2
PBDB-T:di-PDI	4.7	4.3	2,603	-4.1	4.6	3.2	$3.8 \times 10^{-20}$	38.2
PBDB-T:IT-M	10.4	10.1	4,515	-8.5	6.6	4.1	$2.7 \times 10^{-22}$	54.9
PBDB-T:IEICO-4F	5.7	6.0	-	-	-	-	6.7×10 <sup>-23</sup>	51.8

Entries without PCE are systems used for establishing thermodynamic-diffusion relations only, in part because unfavourable energy level alignment leads to poor devices.  ${}^{x}_{\mathcal{H}}T = B$  and  $\chi_{S} = A$  are extracted from miscibility values from SIMS profiles of polymer:NF-SMA bilayers annealed at different temperatures. NF-SMA volume is used as the reference volume in Flory-Huggins theory to extract  $\chi$ . BRT, room temperature. Activation energy E, of diffusion for SMA to diffuse into the polymer. The Pearson coefficients of the Arrhenius fits range from -0.99 to -1, indicating excellent fits overall. Historical fullerene reference system. \*The PCE of FTAZ:IT-M devices and interaction parameters, diffusion coefficient and activation energy of FTAZ:ITIC-4CI.

Table 2 | The conceptual relations of the various equilibrium and dynamic parameters investigated in this work

Figure and	Relation
narameters	

versus χ<sub>H</sub>

Thermodynamic  $(\chi)$ , kinetic (D(T))

Fig. 2c <i>D</i> ( <i>T</i> )	$D(T) = gfv^{0}a^{2}\exp\left(\frac{\Delta S_{d}}{k_{B}}\right)\exp\left(-\frac{\Delta H_{d}}{k_{B}T}\right) = D_{0}\exp\left(-\frac{\Delta H_{d}}{k_{B}T}\right)$	(1)
versus T <sup>-1</sup>	y = y + y = A + B (2)	
Fig. 2d E <sub>a</sub>	$\chi = \chi_{S} + \chi_{H} = A + \frac{B}{T} \tag{2}$	
Vorcus M	$\chi_{H} = -(\varepsilon_{PP} - 2\varepsilon_{PS} + \varepsilon_{SS}) \frac{Z}{2k_{B}T} = \frac{B}{T} = \frac{\Delta H_{m}}{2k_{B}\phi_{S}\phi_{P}} $ (3)	

Thermodynamic  $(\chi)$ , thermal  $(T_{g,c})$ , mechanical  $(E_F)$ Fig.  $4a\chi_{H}$  $\chi_H \propto (\varepsilon_{PP} - 2\varepsilon_{PS} + \varepsilon_{SS})$ (5) versus  $T_{g,c}$  $T_{
m g,c} \propto arepsilon_{
m SS}$ Fig. 4b D<sub>85</sub> (6)  $E_F \propto arepsilon_{ ext{PP}}$ versus  $T_{\rm g,c}$ Fig.  $4c \chi_H$ versus E<sub>F</sub> Fig. 4d D<sub>85</sub> versus E<sub>F</sub>

Kinetic (D(T)), mechanical ( $\tau_r$ )

Fig. 3b 
$$\sigma$$
 versus  $\frac{d\sigma}{dt} = \dot{\sigma} = A \exp\left(\frac{\Delta S_t}{k_B}\right) \exp\left(-\frac{\Delta H_t}{k_B T}\right) \exp\left(\frac{V\sigma}{k_B T}\right)$  (7)  $t$   $\sigma = \sigma_0 \exp\left(-\left(\frac{t}{t_T}\right)^{\beta}\right)$  (8)

 $k_{\rm R}$ , Boltzmann constant;  $\phi$ , volume fraction of different components in a blend where subscripts p and s correspond to polymer and SMA, respectively;  $\Delta H$ , enthalpy change where subscripts m, d and r correspond to that due to mixing, diffusion and relaxation, respectively;  $\Delta S$ , entropy change where subscripts m, d and r correspond to that due to mixing, diffusion and relaxation, respectively; g, geometrical factor  $^{47}$  f, correlation factor;  $v^0$ , attempt frequency; a, lattice parameter; V, activation volume;  $\sigma$ , stress on sample;  $\sigma_0$ , initial stress in sample;  $\beta$ , stretching exponent of the KWW fit.

and molecular dynamics simulations will be useful to assess the ultimate fate of systems that show promising stability over the course of several months and to design superior new materials.

#### Online content

Any methods, additional references, Nature Research reporting summaries, source data, extended data, supplementary information, acknowledgements, peer review information; details of author contributions and competing interests; and statements of data and code availability are available at https://doi.org/10.1038/ s41563-020-00872-6.

Received: 29 April 2019; Accepted: 11 November 2020; Published online: 11 January 2021

#### References

- Zhang, G. et al. Nonfullerene acceptor molecules for bulk heterojunction organic solar cells. Chem. Rev. 118, 3447-3507 (2018).
- Baran, D. et al. Reducing the efficiency-stability-cost gap of organic photovoltaics with highly efficient and stable small molecule acceptor ternary solar cells. Nat. Mater. 16, 363-369 (2016).
- Du, X. et al. Efficient polymer solar cells based on non-fullerene acceptors with potential device lifetime approaching 10 years. Joule 3, 215-226 (2019).
- Cha, H. et al. An efficient, 'burn in' free organic solar cell employing a nonfullerene electron acceptor. Adv. Mater. 29, 1701156 (2017).
- Du, X. et al. Unraveling the microstructure-related device stability for polymer solar cells based on nonfullerene small-molecular acceptors. Adv. Mater. 32, 1908305 (2020).
- Li, N. et al. Abnormal strong burn-in degradation of highly efficient polymer solar cells caused by spinodal donor-acceptor demixing. Nat. Commun. 8,
- Ghasemi, M. et al. Delineation of thermodynamic and kinetic factors that control stability in non-fullerene organic solar cells. Joule 3, 1328-1348
- Wong, H. C. et al. Morphological stability and performance of polymerfullerene solar cells under thermal stress: the impact of photoinduced PC60BM oligomerization. ACS Nano 8, 1297-1308 (2014).
- Zhu, Y. et al. Rational strategy to stabilize an unstable high-efficiency binary nonfullerene organic solar cells with a third component. Adv. Energy Mater. 9, 1900376 (2019).
- 10. Ye, L. et al. Quantitative relations between interaction parameter, miscibility and function in organic solar cells. Nat. Mater. 17, 253-260 (2018).

- Hu, H. et al. Effect of ring-fusion on miscibility and domain purity: key factors determining the performance of PDI-based nonfullerene organic solar cells. Adv. Energy Mater. 8, 1800234 (2018).
- Ma, W. et al. Domain purity, miscibility, and molecular orientation at donor/ acceptor interfaces in high performance organic solar cells: paths to further improvement. Adv. Energy Mater. 3, 864–872 (2013).
- Treat, N. D. et al. Polymer-fullerene miscibility: a metric for screening new materials for high-performance organic solar cells. J. Am. Chem. Soc. 134, 15869–15879 (2012).
- Zhang, C. et al. Understanding the correlation and balance between the miscibility and optoelectronic properties of polymer-fullerene solar cells. J. Mater. Chem. A 5, 17570–17579 (2017).
- Ghasemi, M. et al. Panchromatic sequentially cast ternary polymer solar cells. *Adv. Mater.* 29, 1604603 (2017).
- Li, S. et al. An unfused-core-based nonfullerene acceptor enables high-efficiency organic solar cells with excellent morphological stability at high temperatures. Adv. Mater. 30, 1705208 (2018).
- 17. Yuan, J. et al. Single-junction organic solar cell with over 15% efficiency using fused-ring acceptor with electron-deficient core. *Joule* 3, 1140–1151 (2019).
- Yang, W. et al. Simultaneous enhanced efficiency and thermal stability in organic solar cells from a polymer acceptor additive. *Nat. Commun.* 11, 1218 (2020).
- Ye, L. et al. Miscibility-function relations in organic solar cells: significance of optimal miscibility in relation to percolation. Adv. Energy Mater. 8, 1703058 (2018)
- Treat, N. D., Mates, T. E., Hawker, C. J., Kramer, E. J. & Chabinyc, M. L. Temperature dependence of the diffusion coefficient of PCBM in poly(3-hexylthiophene). *Macromolecules* 46, 1002–1007 (2013).
- Zhao, W. et al. Fullerene-free polymer solar cells with over 11% efficiency and excellent thermal stability. Adv. Mater. 28, 4734–4739 (2016).
- Treat, N. D. et al. Interdiffusion of PCBM and P3HT reveals miscibility in a photovoltaically active blend. Adv. Energy Mater. 1, 82–89 (2011).
- Ye, L. et al. Quenching to the percolation threshold in organic solar cells. *Joule* 3, 443–458 (2019).
- Yazmaciyan, A. et al. Recombination losses above and below the transport percolation threshold in bulk heterojunction organic solar cells. Adv. Energy Mater. 8, 1703339 (2018).
- Bartelt, J. A. et al. The importance of fullerene percolation in the mixed regions of polymer-fullerene bulk heterojunction solar cells. *Adv. Energy Mater.* 3, 364–374 (2013).
- Li, S. et al. Energy-level modulation of small-molecule electron acceptors to achieve over 12% efficiency in polymer solar cells. Adv. Mater. 28, 9423–9429 (2016)
- 27. Flory, P. J. Principles of Polymer Chemistry (Cornell Univ. Press, 1953).
- 28. Rubinstein, M. & Colby, R. H. *Polymer Physics* (Oxford Univ. Press, 2003).
- Batzer, H. & Kreibich, U. Connections between glass transition-temperature, thermodynamic and mechanic values for predicting material properties from the chemical-structure. *Die Angew. Makromol. Chem.* 105, 113–130 (1982).
- 30. Kreibich, U. & Batzer, H. Influence of the segment structure and crosslinking on the glass-transition T<sub>g</sub>-possibilities of predicting T<sub>g</sub> using the values of cohesive energy ecoh. Die Angew. Makromol. Chem. 83, 57–112 (1979).

- Lee, C. J. Correlations of elastic modulus, cohesive energy density and heat capacity jump of glassy polymers. *Polyrn. Eng. Sci.* 27, 1015–1017 (1987).
- Roberts, R. J., Rowe, R. C. & York, P. The relationship between Young's modulus of elasticity of organic solids and their molecular structure. *Powder Technol.* 65, 139–146 (1991).
- Root, S. E., Alkhadra, M. A., Rodriquez, D., Printz, A. D. & Lipomi, D. J. Measuring the glass transition temperature of conjugated polymer films with ultraviolet-visible spectroscopy. *Chem. Mater.* 29, 2646–2654 (2017).
- Sharma, A., Pan, X., Campbell, J. A., Andersson, M. R. & Lewis, D. A. Unravelling the thermomechanical properties of bulk heterojunction blends in polymer solar cells. *Macromolecules* 50, 3347–3354 (2017).
- Balar, N. et al. The importance of entanglements in optimizing the mechanical and electrical performance of all-polymer solar cells. *Chem. Mater.* 31, 5124–5132 (2019).
- Sperling, L. H. Introduction to Physical Polymer Science (John Wiley & Sons, 2005)
- Lodge, T. P. Reconciliation of the molecular weight dependence of diffusion and viscosity in entangled polymers. Phys. Rev. Lett. 83, 3218–3221 (1999).
- Thomas, N. L. & Windle, A. H. A theory of case II diffusion. *Polymer* 23, 529–542 (1982).
- 39. Matsuoka, S. (ed.) Relaxation Phenomena in Polymers (Hanser, 1992).
- Balar, N. & O'Connor, B. T. Correlating crack onset strain and cohesive fracture energy in polymer semiconductor films. *Macromolecules* 50, 8611–8618 (2017).
- 41. Stafford, C. M. et al. A buckling-based metrology for measuring the elastic moduli of polymeric thin films. *Nat. Mater.* **3**, 545–550 (2004).
- Virkar, A. A., Mannsfeld, S., Bao, Z. & Stingelin, N. Organic semiconductor growth and morphology considerations for organic thin-film transistors. *Adv. Mater.* 22, 3857–3875 (2010).
- Kim, J.-S. et al. Tuning mechanical and optoelectrical properties of poly(3-hexylthiophene) through systematic regionegularity control. *Macromolecules* 48, 4339–4346 (2015).
- Collins, B. A. et al. Molecular miscibility of polymer-fullerene blends. J. Phys. Chem. Lett. 1, 3160-3166 (2010).
- 45. Standard Test Methods for Photovoltaic Modules in Cyclic Temperature and Humidity Environments ASTM E1171-15 (ASTM International, 2015).
- White, J. R. On internal stress and activation volume in polymers. J. Mater. Sci. 16, 3249–3262 (1981).
- Mehrer, H. Diffusion in Solids: Fundamentals, Methods, Materials, Diffusion-Controlled Processes (Springer Science & Business Media, 2007).
- Deppe, D. D., Miller, R. D. & Torkelson, J. M. Small molecule diffusion in a rubbery polymer near T<sub>g</sub>: effects of probe size, shape, and flexibility. *J. Polym. Sci., B: Polym. Phys.* 34, 2987–2997 (1996).
- Carpenter, J. H. et al. Competition between exceptionally long-range alkyl sidechain ordering and backbone ordering in semiconducting polymers and its impact on electronic and optoelectronic properties. *Adv. Funct. Mater.* 29, 1806977 (2019).

**Publisher's note** Springer Nature remains neutral with regard to jurisdictional claims in published maps and institutional affiliations.

© The Author(s), under exclusive licence to Springer Nature Limited 2021

NATURE MATERIALS ARTICLES

#### Methods

Materials. FTAZ and HTAZ was provided by the You group with number average molecular mass  $M_n\cong 86$  kg mol<sup>-1</sup>, polydispersity  $D\approx 1.9$  and  $M_n=81.7$  kg mol<sup>-1</sup>,  $D\approx 3$ , respectively, which was synthesized according to the previous literature<sup>50</sup>. P3HT was provided by the McCulloch group with  $M_n\cong 34$  kg mol<sup>-1</sup> and  $D\cong 1.9$ . PTB7-Th was purchased from Solarmer with  $M_n\cong 69$  kg mol<sup>-1</sup> and  $D\cong 2.1$ . PBDB-T was purchased from Solarmer with  $M_n\cong 31$  kg mol<sup>-1</sup> and  $D\cong 2.1$ . PBDB-T2F was purchased from 1-Material with  $M_n\cong 41$  kg mol<sup>-1</sup> and  $D\approx 2.0$ . Y6, EH-IDTBR, IT-M, di-PDI and IEICO-4F were purchased from 1-Material. ITIC-4Cl was provided by the Yan He group. All the solvents and other materials were purchased from Sigma-Aldrich and used without further purification.

Devices. The polymer:NF-SMA devices were fabricated, after extensive optimization, with an inverted structure of indium tin oxide (ITO)/ZnO/ polymer-SMA/MoO<sub>3</sub>/Al. Prepatterned ITO-coated glass with a sheet resistance of around 15  $\Omega$  per square was used as the substrate. ITO substrates were cleaned by sequential sonication in soapy deionized water, deionized water, acetone and isopropanol for 15 min at each step. A zinc oxide (ZnO) electron transport layer was prepared by spin coating at 4,000 r.p.m. from a ZnO nanoparticle solution after an ultraviolet-ozone (UV-O<sub>3</sub>) treatment for 20 min. The ZnO coated substrates were annealed at 150 °C for 30 min. The polymer:NF-SMA active layers were spin coated from at least 3 h stirred solutions in a nitrogen-filled glovebox to obtain thicknesses of roughly 100 nm. Ink formulations of solutions used for casting of the active layers are summarized in Supplementary Tables 1 and 2. The post-annealing of polymer:NF-SMA films was performed in a nitrogen-filled glovebox at an elevated temperature for 10 min. The films then were transferred to a vacuum thermal evaporator. A thin layer (10 nm) of MoO<sub>3</sub> was deposited as the anode interlayer under vacuum followed by 80-100 nm of Al as the top electrode. Evaporation shadow masks were used to fabricate rectangular devices with 1.38 × 5.0 mm<sup>2</sup> dimensions. For device characterizations, J-V characteristics were measured under AM1.5G light (100 mW cm<sup>-2</sup>) using a Class AAA Newport solar simulator. The light intensity was calibrated using a standard Si diode (with KG5 filter, purchased from PV Measurement) to bring spectral mismatch to unity. A forward scanning from -1 V to +1.2 V with a voltage step of 0.02 V and a scan speed of 50 mV s<sup>-1</sup> was used. The dwell time is around 0.4 s. All J-V characteristics were recorded in a nitrogen-filled glovebox with the environmental temperature maintained at roughly 25 °C. The shelflife measurements were performed on the devices stored under the dark condition in a nitrogen-filled glovebox. *J-V* characteristics were recorded using a Keithley 236 source meter unit. Typical cells have a device area of 6.90 mm<sup>2</sup>, which is defined by a metal mask with an aperture aligned with the device area. The devices area was measured using a calibrated Nikon visible light microscope.

DSC measurements. Neat materials used for DSC tests are dissolved in chlorobenzene (CB) at the same temperatures used for device processing with  $15\,\mathrm{mg\,ml^{-1}}$  total concentration. The overnight dissolved solutions were drop-cast on precleaned glass slides that were subsequently annealed at 80 °C for 20 min to remove the residual solvents remained in the sample. The dried films were transferred to the aluminium pans and sealed before DSC measurements. To increase the temperature resolution in DSC measurements, a heating rate of  $3\,^{\circ}\mathrm{C\,min^{-1}}$  was used for neat NF-SMA. Other DSC thermograms are collected with  $10\,^{\circ}\mathrm{C\,min^{-1}}$  unless otherwise mentioned.

**DMA measurements.** The sample preparation of DMA has been discussed in more detail in the literature<sup>37</sup>. The solution of the neat polymer (in chloroform) was drop-cast, in an  $\rm N_2$  filled glovebox, on a glass fibre mesh cut at 45°. This ensures that the applied load under the tension mode acts on the polymer trapped in the voids instead of the fibres themselves. The samples were preheated up to 80 °C to remove the residual solvents trapped in the films. The temperature sweep scans were performed at the oscillating strain of 0.1% at the frequency of 1 Hz and the temperature ramp of 3 °C min $^{-1}$ . The stress relaxation data was collected, at each temperature, from a step-strain experiment under 1% tensile strain for 10 min followed by a 15 min recovery.

Instruments. DSC measurements of the materials was done by TA Discovery DSC using Tzero pans. The SIMS characterizations were carried out in a time-of-flight (TOF) SIMS (ION–TOF V) at North Carolina State University (NCSU). TOF–SIMS experiments were performed using an ION–TOF–SIMS V instrument equipped with a bismuth liquid metal ion gun, Cs+ sputtering gun and an electron flood gun for charge compensation. Dual-beam dynamic SIMS mode was used to provide high depth resolution and chemical resolution simultaneously, where  $Bi_3^+$  was used as the primary ion and  $Cs^+$  was used as the sputtering source. The sputtering ions with an energy of  $10\,\mathrm{keV}$  for thick polymer films and  $3\,\mathrm{keV}$  for thin polymer films were used to sputter the organic interfaces. Both bismuth and caesium ion columns are orientated at  $45^\circ$  with respect to sample surface normal. The analysis chamber pressure is maintained below  $5.0\times10^{-9}\,\mathrm{mbar}$  to avoid contamination of the surfaces to be analysed. DMA tests were performed on DMA 850 (TA Instruments) under an  $N_2$  environment.

Miscibility and  $\chi$  determination. To convert the weight to volume fraction we assumed donor polymers and NF-SMA have the same density of  $1.15\,\mathrm{g\,cm^{-3}}$ . By monitoring the F<sup>-</sup>, Cl<sup>-</sup> or CN<sup>-</sup> ions or molecular fragment that selectively traces NF-SMA, we can accurately obtain the volume fraction of NF-SMA in the polymer-rich layer. The equilibrium compositions extracted from SIMS profiles can be converted to  $\chi$  by using a generalized Flory–Huggins framework to simulate and parameterize the phase behaviour<sup>51</sup>.

Molecular dynamics simulations. Molecular dynamics simulations were performed with the GROMACS 2019 software suite52. Non-bonded parameters for the SMA were obtained from the OPLS-AA force field53. Parameters for bonds and angles were also drawn for the OPLS-AA force field, with the exception of the partial charges (CM5) and inter-moiety dihedral potentials, which were determined by density functional theory calculations at the ωB97XD/6-311G(d,p) level and the automatic fitting option; Gaussian 16 was used for the density functional theory calculations, and the ω parameter was optimally tuned for each molecule<sup>54</sup>. Systems for the molecular dynamics evaluations were prepared following previously reported methods<sup>55</sup>; the NPT (constant number of particles N, constant pressure P, and constant temperature T) compression steps used a temperature coupling constant of 0.1 ps and a velocity rescaling thermostat, and a pressure coupling constant of 2 ps with the Berendsen barostat. Hydrogen-containing bonds were constrained using the linear constraint solver to their equilibrium values. Equilibrium was achieved after 2 ns in the NVT (constant number of particles N, constant volume V, and constant temperature T) ensemble and a further 2 ns in the NPT ensemble, both at 298 K. The systems were then annealed to 550 K, allowed to run at equilibrium for 10 ns and then cooled to 298 K. After this second compression, the amorphous systems were allowed to run at equilibrium for another 10 ns. Confirmation that equilibrium was achieved at each stage was monitored through the density and potential of each system. Equilibration and production NPT steps used the Parrinello-Rahman barostat and the Nose-Hoover thermostat. These equilibrated systems were then used to evaluate the thermal transitions by evaluating the density versus temperature and heat capacity versus temperature.

**Materials used.** The full names of the materials used in this paper were as follows: P3HT: poly(3-hexylthiophene-2.5-diyl)

FTAZ: poly[4-(5-(4,8-bis(3-butylnonyl)benzo[1,2-b:4,5-b']dithiophen-2-yl) thiophen-2-yl)-2-(2-butyloctyl)-5,6-difluoro-7-(thiophen-2-yl)-2H-benzo[d] [1,2,3]triazole]

 $\label{eq:htmap} HTAZ: poly[4-(5-(4,8-bis(3-butylnonyl)benzo[1,2-b:4,5-b']dithiophen-2-yl) thiophen-2-yl)-2-(2-butyloctyl)-7-(thiophen-2-yl)-2H-benzo[d][1,2,3]triazole]$ 

PBDB-T: poly[(2,6-(4,8-bis(5-(2-ethylhexyl)thiophen-2-yl)-benzo[1,2-b:4,5-b'] dithiophene))-alt-(5,5-(1',3'-di-2-thienyl-5',7'-bis(2-ethylhexyl)benzo[1',2'-c:4',5'-c'] dithiophene-4,8-dione)]

PTB7-Th: poly[4,8-bis(5-(2-ethylhexyl)thiophen-2-yl)benzo[1,2-b;4,5-b] dithiophene-2,6-diyl-alt-(4-(2-ethylhexyl)-3-fluorothieno[3,4-b] thiophene-)-2-carboxylate-2-6-diyl)]

PBDB-T-2F: poly[(2,6-(4,8-bis(5-(2-ethylhexyl-3-fluoro)thiophen-2-yl)-benzo] [1,2-b:4,5-b'] dithiophene))-alt-(5,5-(1',3'-di-2-thienyl-5',7'-bis(2-ethylhexyl) benzo[1',2'-c:4',5'-c'] dithiophene-4,8-dione)

Y6: 2,2'-((2Z,2'Z)-((12,13-bis(2-ethylhexyl)-3,9-diundecyl-12,13-dihydro-[1,2,5]thiadiazolo[3,4-e]thieno[2',3':4',5']thieno[2',3':4,5] pyrrolo[3,2-g]thieno[2',3':4,5]thieno[3,2-b]indole-2,10-diyl)bis(methanylylidene)) bis(5,6-difluoro-3-oxo-2,3-dihydro-1<math>H-indene-2,1-diylidene))dimalononitrile

 $EH-IDTBR: (Z)-5-\{[5-(15-[5-[(Z)-(3-ethyl-4-oxo-2-thioxo-1,3-thiazolidin-5-ylidene)methyl]-8-thia-7.9-diazabicyclo[4.3.0]nona-1(9),2,4,6-tetraen-2-yl\}-9,9,18,18-tetrakis(2-ethylhexyl)-5.14-dithiapentacyclo[10.6.0.03,10.04,8.013,17] octadeca-1(12),2,4(8),6,10,13(17),15-heptaen-6-yl)-8-thia-7.9-diazabicyclo[4.3.0] nona-1(9),2,4,6-tetraen-2-yl]methylidene]-3-ethyl-2-thioxo-1,3-thiazolidin-4-one$ 

di-PDI: 2,2',9,9'-tetrakis(1-pentylhexyl)-[5,5'-bianthra[2,1,9-*def*:6,5,10-*d'e'f'*] diisoquinoline]-1,1',3,3',8,8',10,10'(2H,2'H,9H,9'H)-octone

IT-M: 3,9-bis(2-methylene-((3-(1,1-dicyanomethylene)-6/7-methyl)-indanone))-5,5,11,11-tetrakis(4-hexylphenyl)-di thieno[2,3-d:2',3'-d']-s-indaceno[1,2-b:5,6-b']dithiophene

 $\label{eq:energy} IEICO-4F: 2,2'-((2Z,2'Z)-(((4,4,9,9-tetrakis(4-hexylphenyl)-4,9-dihydro-sin daceno[1,2-b:5,6-b']dithiophene-2,7-diyl)bis(4-((2-ethylhexyl)oxy)thiophene-5,2-diyl))bis(methanylylidene))bis(5,6-difluoro-3-oxo-2,3-dihydro-1$H-indene-2,1-diylidene))dimalononitrile$ 

**Reporting Summary.** Further information on research design is available in the Nature Research Reporting Summary linked to this article.

#### Data availability

The data represented in Fig. 3a,b are provided with the paper as source data. Other datasets generated and/or analysed during the current study are available from the corresponding authors upon request.

#### Code availability

The code used for the simulation of the Flory–Huggins phase diagram is available from the corresponding author upon request.

#### References

- Alkhadra, M. A. et al. Quantifying the fracture behavior of brittle and ductile thin films of semiconducting polymers. *Chem. Mater.* 29, 10139–10149 (2017).
- Kozub, D. R. et al. Polymer crystallization of partially miscible polythiophene/ fullerene mixtures controls morphology. *Macromolecules* 44, 5722–5726 (2011).
- Abraham, M. J. et al. GROMACS: high performance molecular simulations through multi-level parallelism from laptops to supercomputers. *SoftwareX* 1-2, 19–25 (2015).
- 53. Jorgensen, W. L., Maxwell, D. S. & Tirado-Rives, J. Development and testing of the OPLS all-atom force field on conformational energetics and properties of organic liquids. J. Am. Chem. Soc. 118, 11225–11236 (1996).
- 54. Frisch, M. J. et al. Gaussian 16 Rev. C.01 (Wallingford, 2016).
- Ryno, S. M. & Risko, C. Deconstructing the behavior of donor-acceptor copolymers in solution & the melt: the case of PTB7. *Phys. Chem. Chem. Phys.* 21, 7802–7813 (2019).

#### Acknowledgements

Y.Q., Z.P., H.H., H.A. and initial work by M.G. was supported by Office of Naval Research (ONR) grant no. N000141712204 and KAUST's Center Partnership Fund (no. 3321). N.B. and B.T.O. acknowledge support by a National Science Foundation (NSF) grant (no. CMMI-1554322). T.K., A.A. and recent work by M.G. was supported by NCSU start-up funds to A.A., J.R. and W.Y. acknowledge support by an NSF grant (no. CBET-1639429). C.R. and W.M. acknowledge the support of the ONR (N00014-18-1-2448) and the NSF under Cooperative Agreement no. 1849213; supercomputing resources were provided by the Department of Defense (DoD) through the DoD High-Performance Computing Modernization Program (project no. ONRDC40433481) and by the University of Kentucky Information Technology Department and Center for Computational Sciences. SIMS measurements were performed at the Analytical Instrumentation Facility at NCSU, which is partially supported by the State of North Carolina and the National Science Foundation. C. Zhou is acknowledged for providing support for SIMS measurements. The DSC instrument was purchased with UNC-GA ROI funds. C. Zhu, A. Hexemer and C. Wang of the ALS provided instrument maintenance. E. Gomez and J. Litofsky are acknowledged for providing the initial

Flory–Huggins program code. L. Ye and M. Balik (NCSU) are acknowledged for fruitful discussion and input. A. Dinku is acknowledged for maintaining shared ORaCEL facilities and sharing some PBDB-T2F:Y6 stability data for reference. F. He and T. Zhao are acknowledged for help with attaining molecular weight data via high temperature gel permeation chromatography. H. Yan is acknowledged for providing ITIC-4Cl NF-SMA. I. Angunawela is acknowledged for performing complementary shelflife measurements of P3HT:EH-IDTBR devices.

#### **Author contributions**

H.A. and B.T.O. conceived the scientific framework with the help of M.G. M.G. designed experimental protocols, coordinated the experimental work, performed the SIMS, DSC measurements and analysed the SIMS and DSC data with the help of Z.P. Z.P. performed the complementary SIMS measurements of P3HT:NF-SMA. M.G. fabricated solar cell devices and performed subsequent stability tests with the help of H.H., T.K. and Y.Q., and with supervision by A.A. B.T.O. and N.B. designed the mechanical test experiments. N.B. prepared the films needed for mechanical test measurements and performed DMA and elastic modulus measurements. H.H. fabricated the complementary FTAZ:IT-M devices. J.J.R. synthesized the FTAZ polymers, supervised by W.Y. M.B. synthesized P3HT, supervised by I.M. W.M. performed molecular dynamics simulations, supervised by C.R. M.G., H.A. and B.T.O. drafted the paper. All authors contributed to the editing and interpretation.

#### **Competing interests**

The authors declare no competing interests.

#### Additional information

Supplementary information is available for this paper at https://doi.org/10.1038/s41563-020-00872-6.

Correspondence and requests for materials should be addressed to B.T.O. or H.A.

**Peer review information** *Nature Materials* thanks Mats Andersson, Andrew T. Kleinschmidt, Darren Lipomi and the other, anonymous, reviewer(s) for their contribution to the peer review of this work.

Reprints and permissions information is available at www.nature.com/reprints.

# natureresearch

Corresponding author(s): Harald Ade and Brendan T. O'Connor

## Solar Cells Reporting Summary

Nature Research wishes to improve the reproducibility of the work that we publish. This form is intended for publication with all accepted papers reporting the characterization of photovoltaic devices and provides structure for consistency and transparency in reporting. Some list items might not apply to an individual manuscript, but all fields must be completed for clarity.

For further information on Nature Research policies, including our data availability policy, see Authors & Referees.

#### Experimental design

1.	Dimensions		
	Area of the tested solar cells	∑Yes ☐ No	Area of the tested solar cells is provided in Methods section.
	Method used to determine the device area	Yes No	Calibrated Nikon visible light microscope is used to determine the device areas. The information can be found in Methods section.
2.	Current-voltage characterization		
	Current density-voltage (J-V) plots in both forward and backward direction	Yes No	We have not included the J-V curves of our organic solar cells in the manuscript as our study focuses on polymer physics and structure-function relation.
	Voltage scan conditions For instance: scan direction, speed, dwell times	Yes No	Voltage scan conditions are provided in Methods section.
	Test environment For instance: characterization temperature, in air or in glove box	Yes No	This information is provided in the caption of Fig. 1 and Methods section.
	Protocol for preconditioning of the device before its characterization	Yes	No preconditioning of the devices were used in our study.
	Stability of the J-V characteristic Verified with time evolution of the maximum power point or with the photocurrent at maximum power point; see ref. 7 for details.	Yes No	Time evolution of the maximum power point vs. shelflife time is presented in Fig. 1c.
3.	Hysteresis or any other unusual behaviour		
	Description of the unusual behaviour observed during the characterization	Yes No	We didn't observe the hysteresis behavior in our organic solar cells.
	Related experimental data	Yes No	We did not observe any unusual behavior in our organic solar cells.
1.	Efficiency		
	External quantum efficiency (EQE) or incident photons to current efficiency (IPCE)	Yes No	EQE data is not included as EQE is not relevant to the polymer physics discussion presented in our work.
	A comparison between the integrated response under the standard reference spectrum and the response measure under the simulator	Yes No	These measurements have not been performed as they are not relevant to this study.
	For tandem solar cells, the bias illumination and bias voltage used for each subcell	Yes No	We did not report any tandem devices in this study.
5.	Calibration		
	Light source and reference cell or sensor used for the characterization	Yes No	
	Confirmation that the reference cell was calibrated and certified	Yes No	This information is provided in Methods section.

	2		
	\$		
	3		
	Ē	÷	
	3		
g	\		
		-	
			۰

	Calculation of spectral mismatch between the	X Yes	This information is provided in Methods section.
	reference cell and the devices under test	∐ No	
5.	Mask/aperture		
	Size of the mask/aperture used during testing	X Yes No	The mask size during testing is provided in Methods section.
	Variation of the measured short-circuit current density with the mask/aperture area	☐ Yes ☑ No	These measurements have not been performed as we did not aim to develop new devices or claim record-efficiency.
7.	Performance certification		
	Identity of the independent certification laboratory that confirmed the photovoltaic performance	☐ Yes ☑ No	The photovoltaic performance of our organic solar cell devices has not been confirmed from independent certification laboratories, as we did not aim to claim record-efficiency.
	A copy of any certificate(s)  Provide in Supplementary Information	☐ Yes ☑ No	N/A
3.	Statistics		
	Number of solar cells tested	Yes No	At least six devices have been tested for each system.
	Statistical analysis of the device performance	X Yes No	We have included the average and max power conversion efficiency and average device characteristics in Table S1 and Table S2.
Э.	Long-term stability analysis		
	Type of analysis, bias conditions and environmental conditions For instance: illumination type, temperature, atmosphere humidity, encapsulation method, preconditioning temperature	X Yes No	The information regarding to the type of the stability measurement and environmental conditions is provided in the Methods section.